Well-aligned, ordered, nanocolumnar, Cu–Si thin film as anode material for lithium-ion batteries

Deniz B. Polat [a], Ozgul Keles [a, *], K. Amine [b, c]

[a] Department of Metallurgical and Materials Engineering, Istanbul Technical University, Maslak, Istanbul 34469, Turkey
[b] Chemical Sciences and Engineering Division, Argonne National Laboratory, 9700 South Cass Avenue, Argonne, Illinois 60439, USA
[c] Chemistry Department, Faculty of Science, King Abdulaziz University, Jeddah, Saudi Arabia

HIGHLIGHTS

- Well-aligned, ordered nanocolumnar CuSi thin film is formed via OAD method.
- In-situ dilatometry is done to measure the expansion of the CuSi thin film anode.
- Long evaporation duration leads broadening of the nanocolumns.
- Homogeneous distributions of porosity and Cu enhance the cyclability of the Si.

ARTICLE INFO

ABSTRACT

Nanocolumnar composite Cu–Si films were produced as anodes using an oblique angle electron beam co-evaporation method. Two evaporation durations were used to yield different film thicknesses: thin ($<250 \pm 100$ nm) and thick ($>400 \pm 100$ nm). The structural and morphological properties of these Cu–Si films were characterized using X-ray diffraction and scanning electron microcopy. Galvanostatic half-cell electrochemical measurements were conducted over a voltage range of 50 mV–2.5 V using Li as a counter electrode and the Cu–Si films as anodes. The results demonstrated that the thin film has homogeneously distributed nanocolumns and yielded good cyclability upto 100 cycles with high capacity retention; by contrast, the thick film has an inhomogeneous porous structure and exhibited poor cyclability. The reason for the better electrochemical performance of the thin film was determined by X-ray photoelectron spectroscopy (XPS) at different states of charge. Moreover, in-situ electrodilatometric analysis during the galvanostatic test of the thin films measured the ongoing volumetric changes upon cycling.

© 2014 Elsevier B.V. All rights reserved.

1. Introduction

The commercial graphite anode is widely used in the lithium-ion battery due to its stable cycling performance [1]. Unfortunately, its relatively low specific capacity (372 mA h g^{-1}) [2] limits its use in lithium-ion batteries requiring high power and high energy density [3]. Among the alternative electrodes materials under consideration [4–6], silicon, with the highest theoretical specific capacity (3579 mA h g^{-1} for $Li_{15}Si_4$, at room temperature), is considered as having the most potential to meet the demands for the transportation applications. However, this anode undergoes a

high volume expansion (400%) during cycling, which induces a mechanical stress that results in pulverization or delamination and, hence, a loss of electrical contact and a short cycle life [7]. With the purpose of adressing the drawbacks of the Si anode, researchers have investigated the effects of changes in electrode composition and microstructural morphology. For instance, Huggins et al. [7] reported the use of an inert matrix along with electrochemically active metallic material (Si, in that case). Besenhard et al. [3,8,9] and Yang et al. [4] further investigated the use of metallic alloys as the anode material. They found that during lithiation, the electrochemically active atoms react with Li$^+$ and form a lithiated product embedded in the non-electrochemically active metallic matrix, which acts as a buffer to suppress the volumetric expansion due to Li$_x$Si formation. The reduced volume expansion has already been demonstrated in the binary intermetallic M_xSi_y (M = Cu, Ni, Co, Sb,

Ag, and Fe) [3,4,7–9]. Of these candidates, Cu_3Si alloys are the most promising because they have a low contact resistance, high electrical conductivity and a high mechanical tolerance to volume change [10,11].

The reaction mechanism of nano-sized Cu_3Si particles with Li/Li^+ has been studied by in-situ and ex-situ techniques. At the beginning of the electrochemical reaction in the first cycle, Si particles react with Li^+ to form the final lithiated product (Eq. (1)).

$$xLi^+ + xe^- + Cu_3Si \rightarrow Li_xSi + 3Cu \qquad (1)$$

During this initial reaction, nanosized Cu particles are extruded from the pristine unit cell and form a conductive matrix that buffers the volume expansion due to the formation of Li_xSi_y particles. Therefore, the presence of nano-sized Cu particles, due to their ductile and electrical conductive properties, was believed to improve the cyclic behavior of the electrode [12]. To date, different methodologies have been used to fabricate Cu_3Si electrodes with various sizes and microstructural morphology [11,13,14]. However, galvanostatic test results revealed that such nano-particle electrodes do not improve the electrochemical performance of the anode, definitely. Because the increased surface area of the nano-particles provides higher surface energy, thereby they merge together during cycling (electrochemical sintering) to form dense blocks unable to take part in the electrochemical reaction [15]. Therefore, this particle–particle interaction should be avoided not only compositionally but also geometrically.

The production of Cu–Si nanocolumns, due to their unique morphology, could prevent "the electrochemical sintering" problem. The interstitial space among these nanocolumns is expected to avoid sintering during electrochemical cycling and increase the mechanical tolerance against volume change, hence the anode service life. Moreover, the free space among the nanocolumns creates an easy route for the electrolyte to access the entire surface and decrease the polarization, which, in turn, improves the capacity retention of the electrode [16].

In this work, we produced two anodes with nanocolumn Cu–Si films of different thicknesses ("thin," $<250 \pm 100$ nm, and "thick," $>400 \pm 100$ nm). They were fabricated by a one-step production technique, oblique angle deposition (OAD) on a Cu substrate. This process poses no risk from having to handle flammable, explosive, or carcinogenic metal nanoparticles [17]. Moreover, a binder or conductive additive is not required to deposit nanocolumnar-structured material. This ensures the direct electron transport of the intermetallic to the current collector and, hence, a fast Li^+ diffusion through the adjustable, small diameters of the nanocolumns [18].

The nanocolumn formation mechanism during the OAD method has been studied previously [19,20]. The results indicate that the orientation of the column growth can be controlled by changing the incident flux angle under low pressure, since electron beam deposition is a line-of-sight process. The columns are formed when the evaporated particle flux strikes the substrate under a highly oblique angle (normally, $\Theta \geq 80°$). Karabacak et al. [19] point out that the dominant processes to control OAD are self-shadowing at the atomic scale and surface diffusion. At room temperature deposition, since the surface diffusion rate is low, once the adsorbed atoms nucleate on active sites of the substrate surface, they tend to grow as inclined nanocolumns if such growth is governed by Volmer–Weber or Stranski–Krastanov processes. In this case, factors such as the surface roughness of the substrate, process duration, and evaporation source composition will have a significant effect on the composition and architecture of the deposited thin film. In turn, these factors are expected to affect the electrochemical performance of the nanocolumn-structured anodes in lithium-ion batteries [19].

The objective of the current study is to evaluate the use of OAD method as an alternative production process to deposit a homogeneous nanostructured Cu–Si film on a Cu discs and to discuss the evaporation duration effect on these films' electrochemical performances when used as anodes in LIB. Anodes composed of such Cu–Si intermetallics are expected to exhibit enhanced performance because of their unique nanostructure.

2. Experimental

Nanocolumnar structured Cu–Si films were deposited on two Cu discs (15.5-mm diameter and 1.5-mm thickness) using an electron beam deposition technique (OAD). The film thickness was varied (<250 nm and between 250nm and 1μm) by use of different process durations (40 min and 120 min, respectively). The deposition of nanocolumnar Cu–Si films on the Cu substrate was realized by the co-evaporation of Cu and Si pellets. These materials were placed in graphite crucibles, prior to evaporation, where the Cu:Si weight ratio was 1:9.

For both anodes, a non porous Cu–Si film was deposited with an incident angle of 0° to reduce the ohmic resistance thereby to delay aggregation in the electrode during cycling. Because, during discharge reaction the non porous layer with Li concentration gradient provides gradual transition to current collector and eliminates stress "singualarity" at the current collector interface. Therefore, more adherent coating would be achieved, leading to a longer cycle life during galvanostatic test. After the non-porous layer, then, inclined Cu–Si nanocolumns were formed when the deposition flux hit the substrate surface with an angle of 80° at room temperature [21]. Taking advantage of the shadowing effect and the limited ad-atom diffusion, one can form inclined nano-columns with homogeneously distributed nanosized porosities. The deposition flux (4 Å s^{-1}) and the substrate temperature (around 30 °C) were held constant during the overall process. The base pressure in the vacuum chamber was 10^{-7} torr. To measure the coating thicknesses and make compositional analyses accurately, we also coated a pure silicon wafer (20×10 mm^2) and a stainless steel coin (15.6-mm diameter, 1-mm thickness) under the same deposition condition.

The weight of the films was measured by using a microbalance before and after the coating process. The amount of active material in the thin films was calculated by multiplying the total weight of the coating with the active material weight percentage as determined from energy dispersive spectroscopy (EDS) analysis (Table 1). This calculated value was used to determine the specific capacity of the anode material. The surface morphology and thickness of the films were investigated by field-emission scanning electron microscopy (FE-SEM, JEOL JSM 7000F). The phases present in the coatings were determined by X-ray diffraction (XRD, Philips PW3710 System) with a 2θ range of 20–100° in steps of 0.05° (with CuKα at 40 kV and 30 mA).

The electrochemical behavior of the films versus Li/Li^+ was determined with a conventional two-electrode system. All half cells were assembled as 2032 coin cells in an Ar-filled glove box (Mbraun, Labmaster) with thin films as test electrodes, pure Li foil as counter electrode, and porous polypropylene film (Celgrad 2400)

Table 1
Composition of the inclined nanocolumnar Cu–Si thin and thick films as determined by EDS.

	Cu (wt%)	Si (wt%)
Thin film	18	82
Thick film	16	84

as separator. The non-aqueous electrolyte used during the experiments was 1 M $LiPF_6$ dissolved in ethylene carbonate (EC) and dimethyl carbonate (DMC) in a 1:1 weight ratio. The cells were tested at room temperature and operated at voltages of 50 mV—2.5 V versus Li/Li^+ with a rate of 50 mA g^{-1}. Cyclic voltammetry (CV) was performed in the potential range of 50 mV—2.5 V versus Li/Li^+ at a scan rate of 0.03 mV s^{-1}, and electrochemical impedance spectroscopy (EIS) was accomplished in the frequency range of 10 mHz—10 kHz at 2.5 V with 5 mV rms, after the 1st, 3rd, and the 25th cycles (Gamry PCI4/750).

The inclined nanocolumnar thin Cu—Si film was analyzed by X-ray photoelectron spectroscopy (XPS). The change in the surface composition and the chemical state of elements present on the thin film surface were determined via XPS analyses of the thin film anode at different states of charge (before cycling, after first discharge, and after first charge).

During the characterization, a Kratos™ Axis Ultra DLD instrument was used for surface analysis. Prior to introduction into the load-lock vacuum chamber of the XPS instrument, all air-sensitive samples were loaded into an inert transfer module interfaced with the instrument. The samples were prepared in an Ar-filled glove box, with no more than 1 ppm O_2 and 1 ppm H_2O. The base pressure of the analysis chamber during these experiments was 3×10^{-10} torr, with operating pressures around 1×10^{-9} torr. Spectra were collected with a monochromatic Al Kα source (1486.7 eV) and a 300 x 700 micron spot size. Peak position was further corrected by referencing the C 1s peak position of adventitious carbon for a sample (284.8 eV, *PHI Handbook of Photoelectron Spectroscopy*), and shifting all other peaks in the spectrum accordingly. Data fitting was done by the program CasaXPS. Each relevant spectrum was fit to a Shirley-type background to correct for the rising edge of the backscattered electrons, which shifted the baseline higher at high binding energies. Peaks were fitted as asymmetric Gaussian/Lorentzians, with 0—30% Lorentzian character.

Finally, we measured the expansion in the inclined nanocolumnar thin Cu—Si film electrode by electrochemical dilatometry [22]. The dilatometer cell (ECD-nano) consisted of two electrodes (working electrode and lithium) separated by a fixed glass frit. An aluminum foil current collector was placed on the top of the upper working electrode and transmitted any height change of the working electrode to a displacement transducer. The dilatometer cell was assembled and filled with electrolyte in an argon-filled glove box (Mbraun, Labmaster). Then, measurements were performed outside the glove box in a test cabinet with a constant temperature (29 ± 0.1 °C), a rate of 200 mA g^{-1}, and a voltage range of 50 mV—2.5 V.

3. Results and discussion

3.1. Effect of evaporation duration on morphological and structural properties

The FE-SEM micrographs in Fig. 1 show surface and cross-sectional views of the as-deposited thin and thick films. It is known that, in OAD methods, during the deposition of Cu and Si atoms on the substrate, atomic shadowing and limited ad-atom diffusion work together to produce a microstructure of small isolated columns. The growth of these columns depends on strong competition and extinction effects. As the process duration increases, this competition and the extinction effects become more severe, which lead to inhomogeneity of the thin film in the plane parallel to the substrate. This distortion in the column morphology can be interpreted as the "broadening" process, which is commonly observed as microstructural defects in the OAD films, when the thickness of the film is increased [23,24].

Fig. 1(a) shows that the thin film has well-aligned nanocolumn arrays with homogeneously distributed porosities as interspaces among them. In contrast, Fig. 1(b) shows that the thick film has smaller inhomogeneously distributed porosities. This difference is due to the effect of evaporation duration on the balance between the atomic shadowing and ad-atom diffusion, as explained previously. As shown by comparison of Fig. 1(c and d), long evaporation duration distorts the homogeneous morphology of the thin film, while the film thickness increases from 100 to 460 nm. Fig. 1(c) indicates that the column diameters are approximately constant,
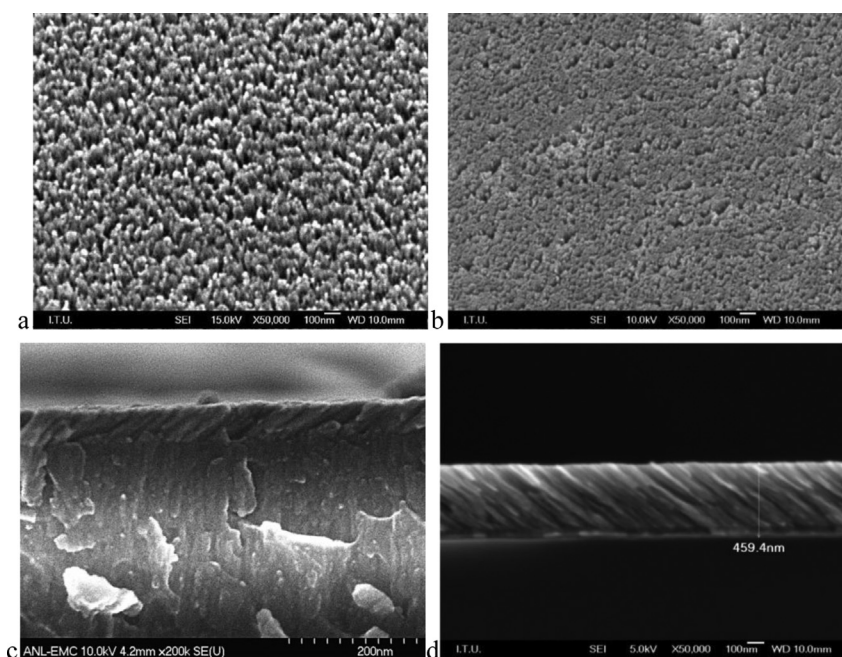

Fig. 1. Surface SEM images of (a) thin and (b) thick Cu—Si films; (c, d) corresponding cross-section SEM images.

around 20 nm in the thin film. As shown in Fig. 1(d) for the thick film, the column diameter increases upto 40 nm along the nano-column height, which is attributed to the broadening that occurs in the longer evaporation process.

The EDS analyses (Table 1) reveal that both films contain similar amounts of silicon (82–84 wt%), independent of their morphologies.

The XRD data indicate that both films consist of Cu_3Si and Si phases, as well as nanosized crystalline or amorphous particles (Fig. 2(a–d)). The XRD data of the Cu–Si films on a Cu disc were compared to those of films deposited on a Si wafer. The results show that the peak at $2\theta = 56.122°$ originates from the Si wafer in the thin film, since there is no such peak for the thin film on Cu substrate (Fig. 2(a and b)). However, the peak at 56.122° is still present in the XRD spectrum of the thick film on the Cu substrate (Fig. 2(a and b)). The latter proves that the long evaporation duration enhances the Si crystal formation.

The presence of the nanocrystalline (α-Si) and amorphous (a-Si) Si particles in the film is critical for the electrochemical performance of the Si-based electrodes since their reactions with Li^+ differ, depending on the cell potential [25–27]. In previous studies, the Li^+ insertion/extraction mechanisms were analyzed by in-situ XRD, SEM, and high-resolution transmission electron microscopy (TEM) [25–28]. The results demonstrate that during Li^+ insertion, the crystal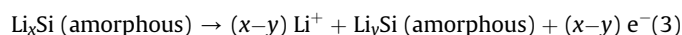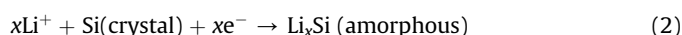 structure of the nanoparticle Si is destroyed and converted into an amorphous metastable structure (Li–Si) according to the "solid state amorphization theory" [27,28], without formation of an intermediate phase. This amorphous lithiated Si phase prevails up to 0.05 V, when a new crystalline compound is formed: $Li_{15}Si_4$ appears at cell potential <0.05 V. Furthermore, during Li^+ extraction, crystalline (on the anodic side) $Li_{15}Si_4$ is converted into both amorphous and crystalline particles, where an internal trapping of Li^+ ion occurs and results in a decrease in the specific capacity delivered by the thin film anode. However, unlike the crystalline Si particles, the amorphous Si particles form merely an amorphous lithiated Si product during transition of Li^+ insertion, which transforms into $Li_{15}Si_4$ at voltages lower than 0.05 V. As long as the lattice expansion can be adequately contained by eliminating the formation of the two-phase region, the amorphous Si particles are advantageous, since Li^+ diffusion paths develop in the amorphous thin film, leading to a higher electrochemical performance during cell cycling.

As mentioned previously, the particle sizes of the Cu–Si electrodes are very important since they directly affect the electrochemical performance of the electrodes. The XRD data show that the thin film has smaller Cu_3Si crystallites than those of the thick film, since the characteristic peak of the Cu_3Si phase ($2\theta = 44.57°$) is broader in the thin film's spectrum. This change in the full width at half maximum of the characteristic peak proves that longer process duration causes particle agglomeration in the thin film, resulting in larger Cu_3Si and Si particles.

3.2. Effect of evaporation duration on electrochemical performance

Fig. 3(a and b) presents the cyclic voltammograms (CV) of electrodes with inclined nanocolumnar thin and thick films. The curves reveal that the current-potential characteristics of the thick Cu–Si film are slightly different from that of of the thin film.

The CV curves of the thin film electrode over three cycles (Fig. 3(a)) show that the peak numbers and intensities differ at each cycle. The first-cycle CV curve of the thin film displays only one reduction peak, around 0.05 V, which is related to the reaction between Li^+ and Si particles to form $Li_{15}Si_4$ particles. Then, during the extraction of Li^+, two anodic peaks (at 0.3 and 0.5 V), related to formation of amorphous and crystalline compounds on the surface of the electrode, are detected [24]. Also evident in Fig. 3(a) an additional cathodic peak around 0.2 V appears in the following two cycles. The presence of this peak indicates that after the first cycle, various Li_xSi_y particles form on the electrode surface. In addition, the peak intensities of the CV curves show a significant decrease with cycle number. Xianhua et al. [29] explain that among all Li–Si intermetallics, the ones having less Li (Li Si or $Li_{12}Si_7$) have the highest formation energy, thus the greatest stability compared to others (Equations (2) and (3)).

$$xLi^+ + Si\,(crystal) + xe^- \rightarrow Li_xSi\,(amorphous) \tag{2}$$

$$Li_xSi\,(amorphous) \rightarrow (x{-}y)\,Li^+ + Li_ySi\,(amorphous) + (x{-}y)\,e^- \tag{3}$$

Once one of these Li-deficient intermetallics is formed (Li Si or $Li_{12}Si_7$), this compound is difficult to dissociate due to its high stability [30], reducing the peak intensities in the following cycles.

The CV curves for the thick film electrode (Fig. 3(b)) are similar to those of the thin film electrode in that there are clear differences in the CV curve shapes between the first and the subsequent cycles. The inhomogeneous morphology of the thick film, which restricts Li^+ diffusion by the electrode surface, has a strong capacitance effect. Thus, a low amount of Li^+ intercalation occurs during the initial discharge reaction. Fig. 3(b) shows that, during the first discharge (Li alloying) of the inhomogeneous thick film, two broad
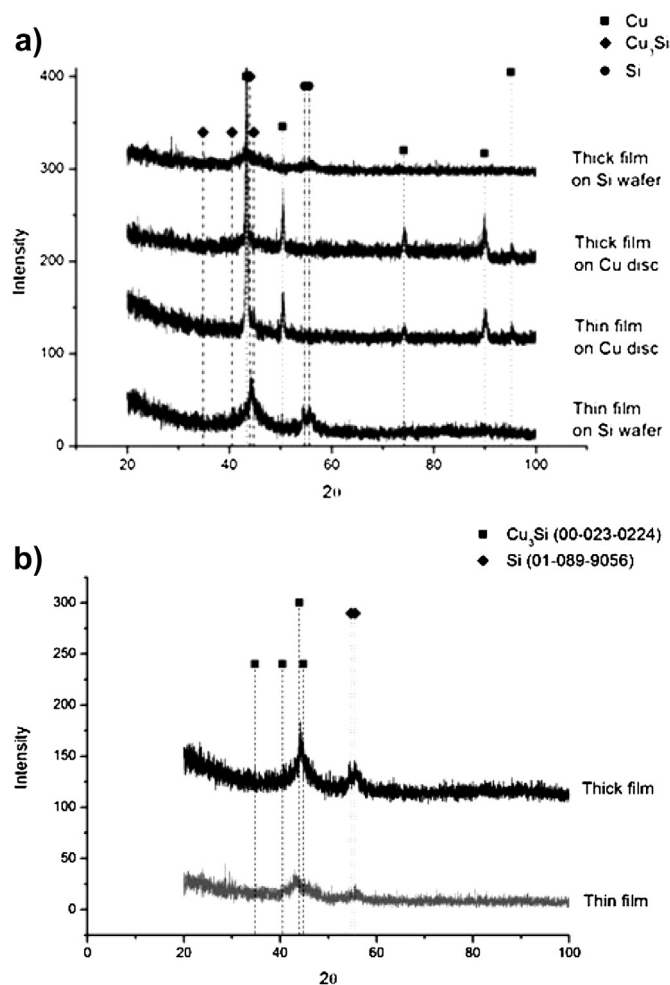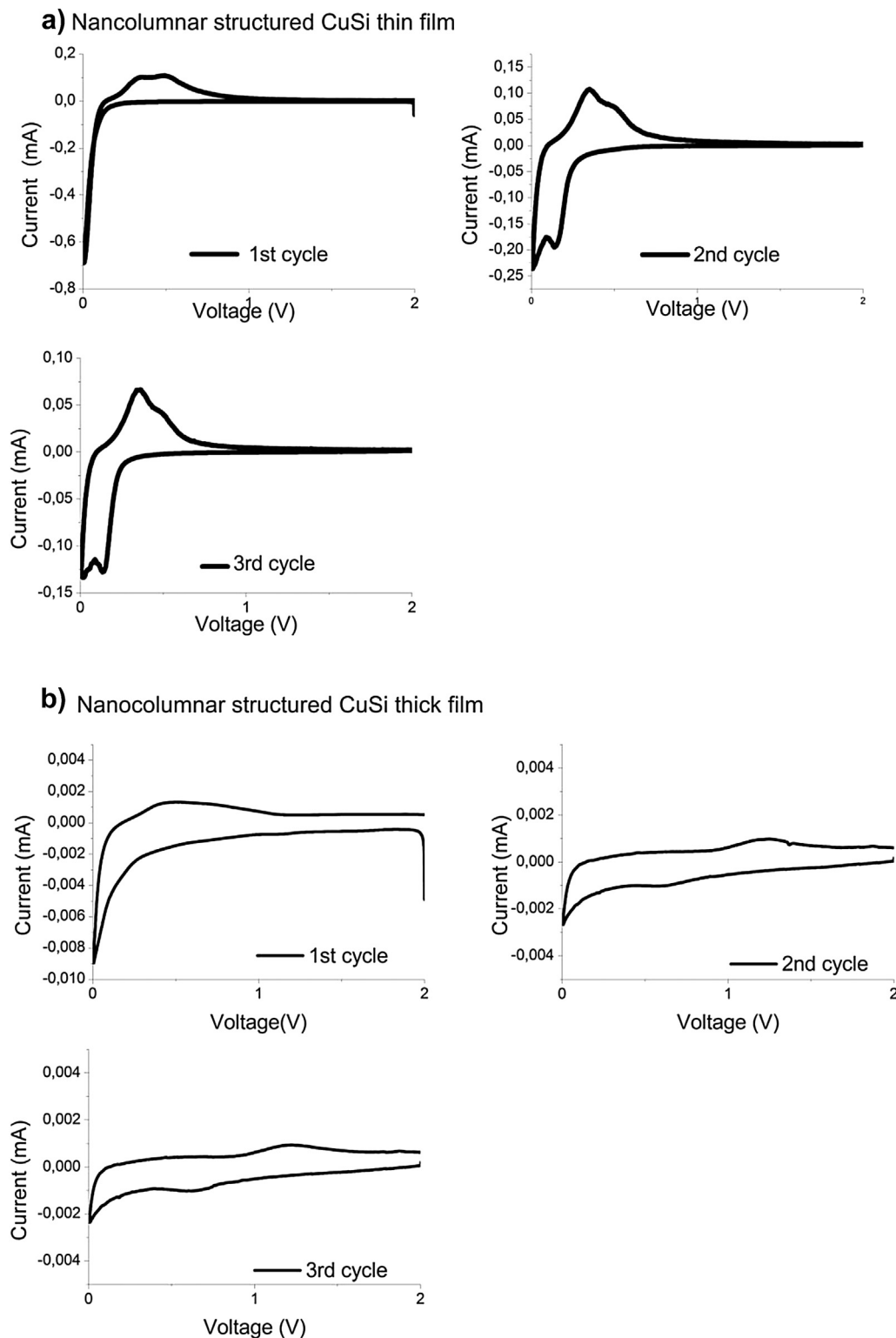

Fig. 2. XRD analyses of the thin and thick Cu–Si films (a) on Si wafers and Cu discs, (b) on Si wafer in detail.

a) Nancolumnar structured CuSi thin film

b) Nanocolumnar structured CuSi thick film

Fig. 3. Cyclic voltammetry profiles of (a) thin and (b) thick Cu—Si film anode during first three cycles.

and one sharp cathodic peaks appear around potentials of 1.2 V, 0.5 V and 0.05 V, respectively. The first cathodic peak is attributed to SEI formation, since it disappears in the following cycles, and the second is related to the lithiation of crystalline (around 0.45 V) and amorphous Si (0.5 V) particles, because this peak is not totally reversible in the anodic side. The other sharp cathodic peak

represents the reduction reaction of Si particles to form Li_xSi alloys. The anodic peaks detected around 1.0 V and 0.05 V indicate that oxidation occurs on the electrode during the delithiation reaction, recovering partially Si particles from the lithiated products. After the first cycle, the cathodic peak around 1.0 V disappears, and a sharp peak forms 0.05 V. A small increase in the current intensity of

this peak (at 0.05 V), after the first cycle, is noted for the thick film, which is attributed to a decrease in the capacitive effect on the electrode due to cracks and pulverization followed by a volume changes. Fig. 3(b) displays that the CV curvature of the 2nd and 3rd cycles are highly overlap, indicating that an irreversible reaction is suppressed by maintaining the equilibrium state after the first cycle; hence, while some reactions occur on the thick Cu—Si film, the SEI film still prevails on the electrode surface after the first discharge reaction.

The CV profiles of both Cu—Si films show similarities with those of thin Si films, previously reported in the literature [31]. This finding suggests that during cycling, the nanoparticle Cu acts as an inactive component, since no particular peak associated with it is detected in Fig. 3. Therefore, it is expected to have a positive effect on the cyclic behavior of the nanocolumnar thin Cu—Si film anode.

Observing a film's electrochemical behavior by means of EIS is a common methodology used by different research groups [12]. It has several advantages. A semicircle extension in the high frequency region demonstrates the impedance caused by the bulk material or interfacial parameters (like SEI formation). Also, a second semicircle present in the high frequency region indicates the charge transfer resistance related to Li^+ interfacial transfer coupled with capacitance resistance of the electrode surface. Finally, an upward slope at the low frequency region proves Li^+ diffusion through the bulk material during the cycling test, and the degree of the slope, if it reaches 45°, implies that Li^+ can easily diffuse in the bulk material.

To further examine the electrochemical behavior of the nanocolumnar thin and thick Cu—Si films, we plotted their impedance data after the 1st, 3rd, and 25th cycles in Fig. 4(a and b). On the 1st cycle of the thick film anode (Fig. 4(b)), two semi-circles are evident, besides an ohmic resistance. The semi-circle at high frequency reveals the SEI formation, and the other shows the charge transfer resistance during lithiation reactions. Moreover, the lack of Warburg impedance in Fig. 4(b) suggests limited Li^+ diffusion in the thick film due to its capacitive behavior. When its capacitive behavior is distorted by a large volumetric change, two semi-circle merge together with a decrease in the ohmic resistance. The reduction of the ohmic resistance can be explained by the enhanced contact of the swollen electrode with the current collector when Li^+ is introduced in it. The formation of one semicircle at high frequency region is related to the generation of a new interface with SEI, due to the inhomogeneous morphology of the film. The inclined slope with 45° seen in Fig. 4(b), indicates that a limited amount of Li^+ has started to diffuse through the anodes once the capacitive effect is decreased during cycling. By contrast, Fig. 4(a) shows that the EIS data for the 1st, 3rd, and the 25th cycles with the thin Cu—Si film anode are close to 45° at low frequency, signifying that Li^+ diffuses during the whole cycling test. In addition after the 1st cycle, a decrease in the arc diameter of the first semicircle is noted in the impedance data of the thin film anode (Fig. 4(a)). It is possible to explain this decrease due to "electrochemical grinding" of the electrodes [28], which is a result of the high volumetric change. In this regard, once the average particle size of the coating is reduced during the cycling test, the surface area of the anode is increased eventually. The high surface area increases the current that passes in the cell and decreases the impedance detected. In that case, the Li^+ diffusion becomes easier, and a better capacity utilization occurs with a higher columbic efficiency. Moreover, this decrease in the impedance of the thin film electrode in further cycles also proves the presence of the "SEI glue effect," which provides electrical conduction among the electrochemically ground particles, resulting from the high volume changes. Since no binder is used during the electron beam deposition, the possible delamination of the small particles from the
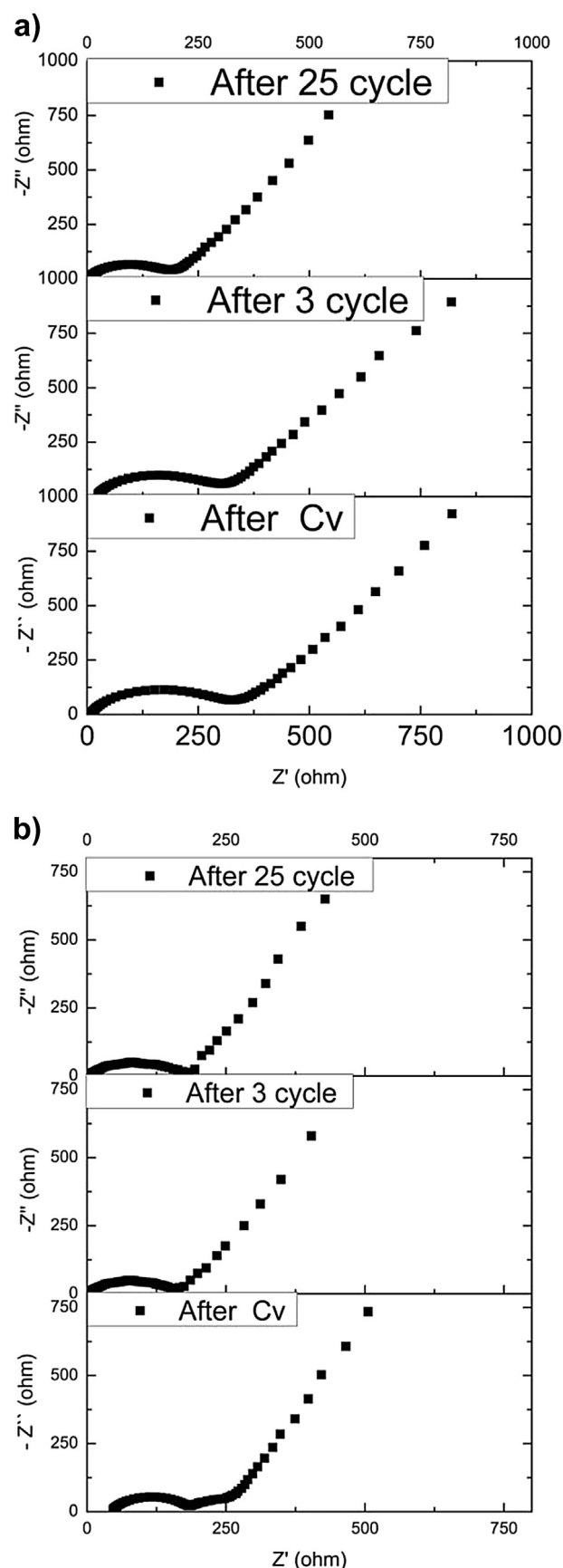

Fig. 4. EIS spectra of (a) thin and (b) thick Cu—Si film after the 1st, 3rd, and 25th cycles.

current collector is mostly prevented due to the SEI layer formation on the electrode surface.

Fig. 5(a and b) displays the insertion and extraction capacities of the thin and thick films, with their coulombic efficiencies, over 100 cycles. Based on the EDS data for Si weight fraction, the theoretical capacities are calculated to be 3579 x 0.82 = 2934.7 mA h g^{-1} for the thin electrode and 3579 × 0.84 = 3006.4 mA h g^{-1} for the thick electrode (where 3579 mA h g^{-1} is the theoretical capacity of Si, assuming the formation of Li$_{3.75}$Si, and the Si fractions provided in Table 1). With respect to these values, the thin film attains 99% of its theoretical capacity (the initial discharge capacity is measured to be 2933.7 mA h g^{-1}), whilst the thick film delivers 1307.5 mA h g^{-1} initially, which is 43% of its theoretical capacity.

On the basis of the structural and the morphological analyses (Figs. 1 and 2), the difference in the initial capacities and the coulombic efficiencies of the electrodes can be better understood. The high first-discharge capacity of the thin film can be explained by the presence of amorphous and nanosized crystalline particles in its well-aligned nanocolumnar structure. This homogeneous morphology provides a highly accessible surface area for Li$^+$ to react with Si, as well as homogeneously distributed porosities among the nanocolumns to suppress the volumetric change during lithiation/delithiation reactions. On the other hand, the increase in the film thickness causes inhomogeneity in its morphology, which limits accessible surface areas for Li$^+$ causing a low initial discharge capacity and results in more Li$^+$ trapping leading to a low Coulombic efficiency. Moreover, the highly crystallized structure and the large particle size of the thick film electrode give rise to a high internal stress in the film and high volumetric changes, hence, deterioration of the film structure and loss of contact with the current collector.

Initially, the coulombic efficiencies for the thin and thick films are 40% and 25%, respectively, then these values rapidly increase and reach 98% and 91% in the 100th cycle (Fig. 5). By contrast the electrode capacities decrease with cycling, reaching 602.3 and 98.4 mA h g^{-1} after 100 cycles, respectively. Knowing that the thin film contains nano-sized Cu$_3$Si and Si crystals with amorphous Si particles (Fig. 2), it is highly possible that an amorphous lithiated compound (single phase) had formed, improving the cycle reversibility. Moreover, the nanosized Cu$_3$Si particles in the thin film can work as a buffer to decrease the mechanical stress that occurs during the lithiation process. These particles can also increase the electrical conductivity, leading to the better capacity retention of the thin film anode. Furthermore, a transition zone between the substrate and the nanocolumns is believed to have promoted the adhesion of the thin film to the current collector, enhancing the cycle life performance. Finally, the SEI layer "glue effect," which gathers all the small electrochemically grounded particles of the thin film together, could also explain its remarkable electrochemical performance for 100 cycles. On the other hand, the thick film delivers only 98.4 mA g^{-1} with 91% coulombic efficiency for 100 cycles. It is still not clear that why the performance of the thick film electrode fades so quickly. The high stress along the columns and the inhomogeneous column size distribution (with
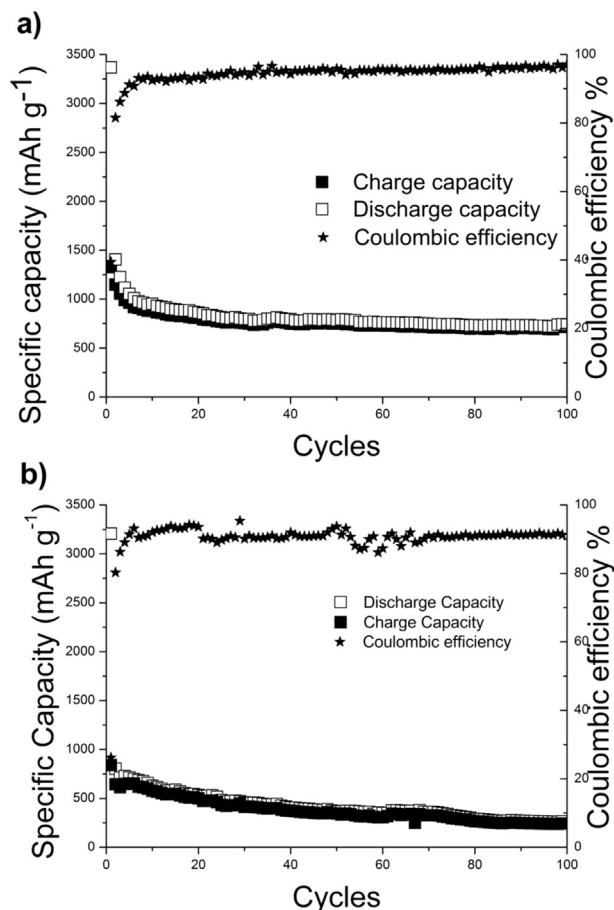

Fig. 5. Specific capacities delivered by (a) thin and (b) thick Cu–Si films upon cycling, with their coulombic efficiencies.
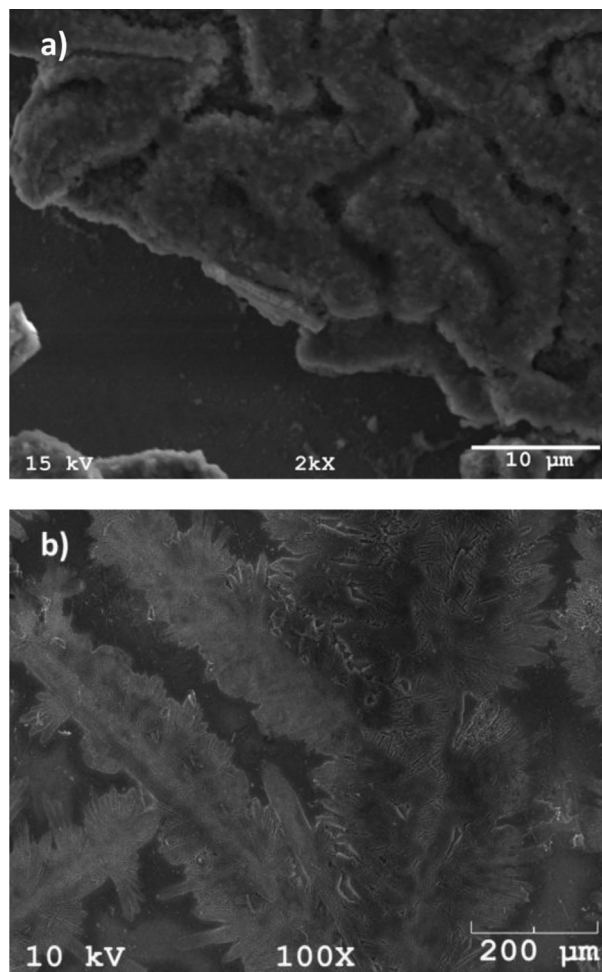

Fig. 6. SEM surface views of (a) thin and (b) thick Cu–Si films after the cycling test.

high Si content) of the thick film could account for its poor cycle life performance, since it is well known that coarse particles are more prone to pulverization than fine ones. Thus, the thick film might experience severe fragmentation and electrical isolation during the charge/discharge reactions, leading to a rapid decay in the capacity, despite the gluing effect of the SEI layer and intermediate non porous film present on the current collector.

Fig. 6(a and b) presents SEM images of both films after the cycling test. The images reveal that in the case of the thin Cu–Si film, electrochemical grinding is partially detected after 100 cycles, whilst for the thick Cu–Si film, severe delamination is clearly evident. The inhomogeneous morphology and the larger particle size of the thick film resulted from the prolonged evaporation duration, which seems to have caused the instability in its electrochemical performance.

3.3. XPS analysis of thin Cu–Si film anode

The CV and EIS analyses showed that SEI layer formation on the electrodes after the first cycle is critical to understanding the electrochemical behavior of the thin film electrode. The change in the thin Cu–Si film surface during the 1st cycle has also been investigated by the XPS method. Since XPS is a surface sensitive analysis technique, the results are expected to reveal the differences in the surface composition at the thin film electrode or solid electrolyte interface, depending of the electrode's state of charge. It should be emphasized that the absence of the binder in these anodes allows for a more straightforward analysis of the SEI formation and the changes in the anode's surface.

The XPS spectra given in Fig. 7 suggest changes on the thin film surface after the first discharge and charge, as expected. On the pristine surface spectrum is the C peak associated with the universal contamination; Si and Cu peaks are also detected. After the first discharge, XPS analyses revealed no Si or Cu peaks, which proves that the SEI layer is thick enough to cover the electrode surface. Furthermore, when the SEI layer composition is investigated more deeply on the discharged electrode, XPS analyses reveal Li–F, C–F, Li–CO₃, O–C=O, C–C, and C=O peaks.

Upon cycling, the C1s and Li1s spectra show some differentiation on the thin film surface. The disappearance of O–C=O peaks on the charged sample indicates the decomposition of lithium carbonate species, since the C1s peak at 290.1 eV is assigned to the carbonate-containing functionalities. However, the prevalence of C–C, C–O, and C=O peaks indicates the presence of the SEI layer on the charged sample. For comparison, the C 1s spectrum of Si anode material was also investigated. The C1s peaks detected around 285.5–289 eV (C–C, C–O, and O–C=O) might demonstrate the presence of PEO (polyethylene oxide) or ether functionalities or lithium alkoxides formed on the charged anode material. These compounds could be derived from a one-electron reduction of diethyl carbonate, ethylene carbonate, or other carbonate products, which are further reduced to form ether, alkoxide, ester, carboxylate, and the lithium oxide products on the SEI present on the anode material. In addition, Fig. 7 reveals small Cu peaks on the
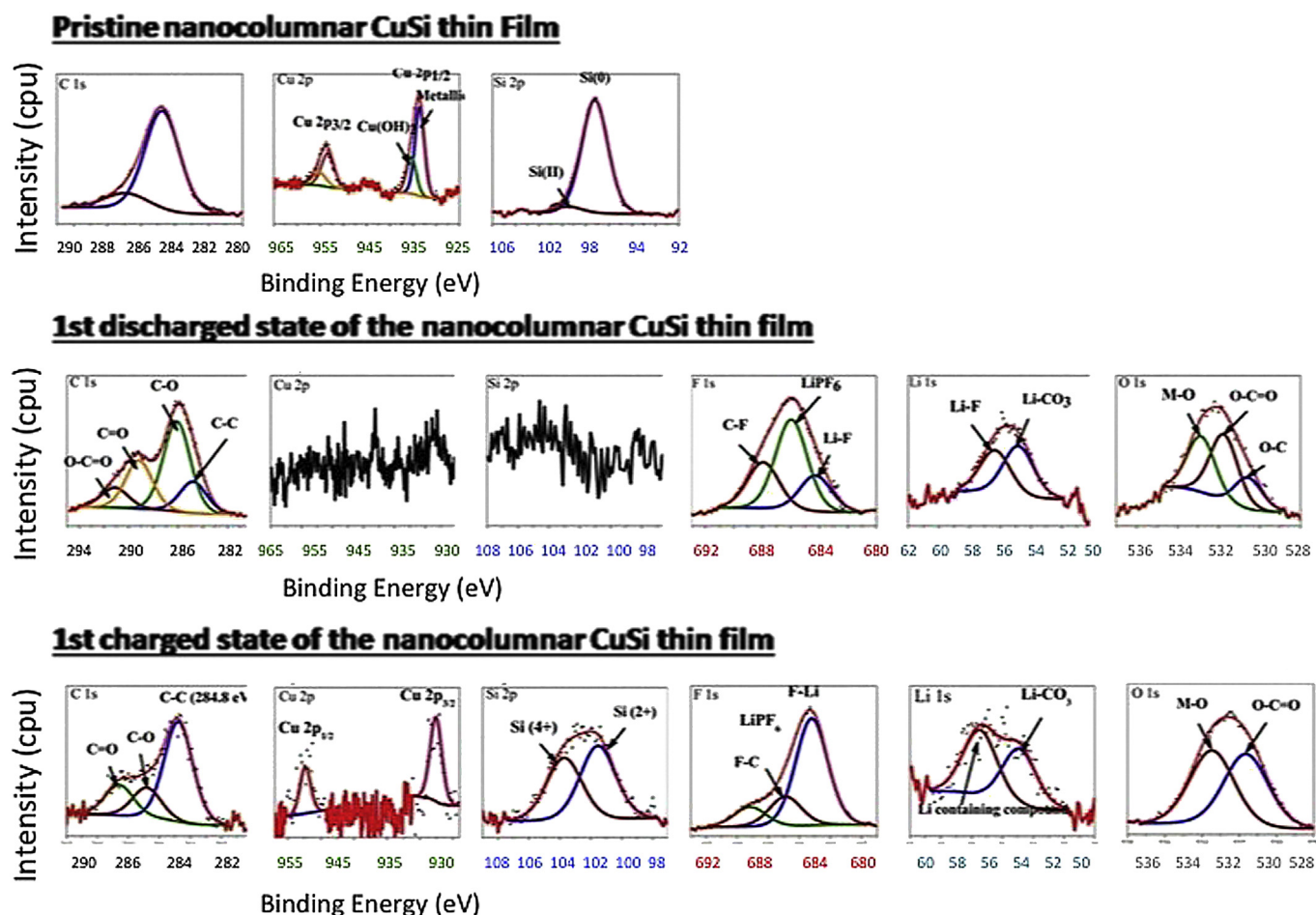

Fig. 7. XPS spectra of Cu 2p, Si 2p, Li 1s, and F1s peaks of the thin Cu–Si film electrode before cycling (pristine), after the first discharge, and after the first charge.

charged samples and no metallic Si peaks. Moreover, XPS data of the charged sample show that Si is present in the oxide film as Si^{2+} and Si^{4+}, indicating that the SEI layer has some products containing these ions, such as Li_xSiO_y.

The XPS results of the thin Cu–Si film (Fig. 7) are similar to those previously reported for the thin Si film, Si nanowires, and Si nanoparticles [32–35]. They reveal that the SEI is primarily composed of the electrolyte reduction products and contains a low amount of Si. The amount of Cu in the thin film seems to have no effect on the SEI film formation, as it is inactive to Li^+. Hence, we believe that the role of Cu in the electrochemical performance of the anodes is mostly a "buffering" effect. Once the SEI forms, it remains on the electrode in the subsequent cycles and suppresses the pulverization of small Si particles generated from the high volume changes due to its "glue effect". Nie et al. [35] observed, by TEM analyses, SEI formation on the Si anode surface after several cycles. This observation is in line with our observations and reveals that the SEI prevails on the electrode and gathers Si nanoparticles together, consistent with our electrochemical test results (Fig. 5(a)).

3.4. Electrochemical dilatometer analysis of thin Cu–Si film anode

We undertook an in-situ electrodilatometric measurement, where the volumetric change of the thin film electrode versus time and the ambient temperature were registered during a galvanostatic test (Fig. 8).

Knowing that the thin Cu–Si film is made of nanosized particles with amorphous structure (Fig. 3), the anode expansion is expected to be isotropic. Thus, the measured height change is believed to show the volumetric change in the thin film during the cycling test. The initial decrease in the height apparent in Fig. 8 during the rest period is due to the creeping of the dilatometer itself, and the subsequent height changes are mainly due to the Li^+ insertion and extraction reactions. Although the reason for the height change in Fig. 8 for the first 3 cycles is not clear, a remarkable volume increase and decrease can be detected after three cycles. This could verify that electrochemical grinding might have occurred initially in the thin film due to the high volume changes, resulting in instabilities of the electrode performance. However, after the 3rd cycle, we can clearly detect that the height of the film increased and decreased during lithium insertion and extraction reactions. In addition, Fig. 8 shows the change of the height versus the ambient temperature,

where a remarkable correlation between the temperature change and the dilatation is noted. This thermal expansion is mainly that of the dilatometer itself, rather than that of the film, which justifies our attempt to keep the temperature stable during the experiment.

The height drift is found to be 6.5 nm h^{-1} through the electrochemical dilatometer analysis, which indicates 200% volumetric change when the thin Cu–Si film is used as anode material.

4. Conclusions

Nanocolumnar Cu–Si films were produced on a substrate by OAD, varying the evaporation durations to give two thicknesses. The outcomes of this study can be summarized as follows:

-The thin film anode having ordered nanocolumns had an initial discharge capacity of 2933.7 mA h g^{-1}, which decreased to 602.3 mA h g^{-1} with 98% coulombic efficiency after 10 cycles and remains at that level for 100 cycles. Structural and morphological analyses showed that the nanosized particles present in the nanocolumns and the homogeneous distribution of porosities in the thin film facilitate Li^+ diffusion within the electrode. Moreover, the additional amount of Cu increased the ductility and the conductivity of the thin film electrode, which resulted in highly stress-tolerant anode formation.
-The thick film anode had an initial discharge capacity of 1307.5 mA h g^{-1}, which decreased gradually to 98.4 mA h g^{-1} with 91% coulombic efficiency after initial cycles and the capacities retained similar for 100 cycles. The inhomogeneous morphology, large particle size, and crystalline Si formation of the thick film resulting from the longer evaporation duration seem to cause instability in the electrode performance and a shorter cycle life.
-Based on XPS analyses, an SEI layer formed on the thin film electrode surface after the first discharge reaction, in which the "glue effect" enhances the cyclability of the electrode. Moreover, based on the XPS analysis of the thin film at different states of charge, the SEI composition depends only on the electrolyte and the active material in the thin film.
-The electrochemical dilatometer measured 200% volume expansion in the thin Cu–Si film anode during a cycling test. This result proves that the electrochemical performance of the anode is improved by using the nanocolumnar thin Cu–Si film anode.
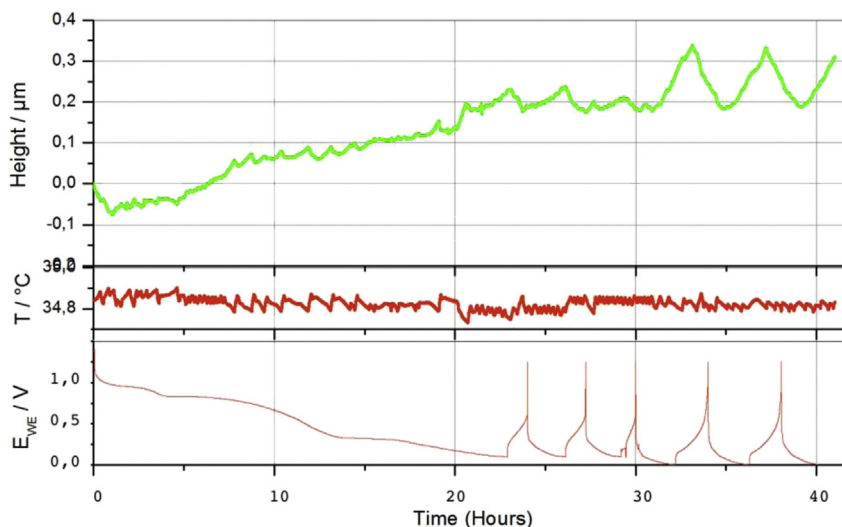

Fig. 8. In-situ electrochemical dilatometer results for the thin Cu–Si film anode.

Acknowledgment

References

[1] W. Hongyu, M. Yoshio, J. Power Sources 93 (2001) 123.
[2] B. Scrosati, Electrochim. Acta 45 (2000) 2461.
[3] J.O. Besenhard, J. Yang, M. Winter, J. Power Sources 68 (1997) 87.
[4] Z. Yang, D. Wang, F. Li, D. Liu, P. Wang, X. Li, H. Yue, S. Peng, D. He, Mater. Lett. 90 (2013) 4.
[5] X. Chen, J.P. Cheng, Q.L. Shou, F. Liu, X.B. Zhang, Cryst. Eng. Comm. 14 (2012) 1271.
[6] C.X. Guo, M. Wang, T. Chen, X.W. Lou, C.M. Li, Adv. Energy Mater. 1 (2011) 736.
[7] J. Wang, I.D. Raistrick, R.A. Huggins, J. Electrochem. Soc. 133 (1986) 457.
[8] J.O. Besenhard, P. Komenda, A. Paxinos, E. Wudy, M. Josowicz, Solid State Ionics 18-19 (1986) 823.
[9] J.O. Besenhard, M. Hess, P. Komenda, Solid State Ionics 40-41 (1990) 525.
[10] H. Cai, D. Tong, Y. Wang, X. Song, B. Ding, J. Alloys Compd. 509 (2011) 1672.
[11] S. Yoon, S.I. Lee, H. Kim, H.J. Sohn, J. Power Sources 161 (2006) 1319.
[12] W.R. Liu, N.L. Wu, D.T. Shieh, H.C. Wu, M.H. Yang, C. Korepp, J.O. Besenhard, M. Winter, J. Electrochem. Soc. 154 (2007) A97.
[13] J.H. Kim, H.J. Sohn, Electrochem. Commun. 7 (2005) 557.
[14] K. Wang, X. He, L. Wang, J. Ren, C. Jiang, C. Wan, Solid State Ionics 178 (2007) 115.
[15] N. Dimov, S. Kugino, M. Yoshio, Electrochim. Acta 48 (2003) 1579.
[16] T. Umeno, K. Fukuda, H. Wnag, N. Dimov, T. Iwao, M. Yoshio, Chem. Lett. 30 (2001) 1186.
[17] D.X. Ye, T. Karabacak, R.C. Picu, G.C. Wang, T.M. Lu, Nanotechnology 16 (2005) 1717.
[18] A. Irrera, E.F. Pecora, F. Priolo, Nanotechnology 20 (2009) 135601.
[19] T. Karabacak, J. Appl. Phys. 96 (2004) 5740.
[20] T. Karabacak, G.C. Wang, T.M. Lu, Mater. Res. Soc. Symp. Proc. 859 (2005). JJ9.5.1-6.
[21] W. Pu, X. He, J. Ren, C. Wan, C. Jiang, Electrochim. Acta 60 (2005) 4140.
[22] L. Ji, Z. Lin, M. Alcoutlabi, X. Zhang, Energy Environ. Sci. 4 (2011) 2682.
[23] M.O. Jensen, M. Brett, J. Appl. Phys. A 80 (2005) 763.
[24] K. Robbie, M.J. Brett, J. Vac. Sci. Technol. A 15 (1997) 1460.
[25] F. Wang, M. Zhao, X. Song, J. Alloys Compd. 439 (2007) 249.
[26] Y.C. Chen, J.M. Chen, Y.H. Huang, Y.R. Lee, H.C. Shih, Surf. Coat. Tech. 202 (2007) 1313.
[27] B.V. Ratnakumar, M.C. Smart, S. Surampudi, in: Battery Conference on Applications and Advances, 2002, p. 273.
[28] C. Nguyen, S.W. Woo, S.W. Song, J. Phys. Chem. C. 116 (2012) 14764.
[29] H. Xianhua, H. Sheju, R. Qiang, Z. Zhiwen, Rare Metal. Mater. Eng. 39 (2010) 2079.
[30] D.T. Shieh, J. Yin, K. Yamamoto, M. Wada, S. Tanase, T. Sakai, J. Electrochem. Soc. 153 (2006) A106.
[31] J.T. Li, J. Swiatowskai, A. Seyeux, L. Huang, M. Maurice, S.G. Sun, P. Marcus, J. Power Sources 195 (2010) 8251.
[32] R.Z. Hu, M.Q. Zeng, M. Zhu, Electrochim. Acta 54 (2009) 2843.
[33] D. Dees, E. Gunen, D. Abraham, A. Jansen, J. Prakash, J. Electrochem. Soc. 152 (2005) A1409.
[34] B. Philippe, R. Dedryvere, J. Allouche, F. Lindgren, M. Gorgio, H. Rensmo, D. Gonbeau, K. Edström, Chem. Mater. 24 (2012) 1107.
[35] M. Nie, D.P. Abraham, Y. Chen, A. Bose, B.L. Lucht, J. Phys. Chem. C. 26 (2013) 13403—13412.